Geophysical Journal (1989) **97**, 295–309

Wave propagation in a vertical transversely isotropic medium: field experiment and model study

C. Kerner, B. Dyer and M. Worthington

Geology Department, Imperial College of Science and Technology Prince Consort Road, London SW7 2BP

Accepted 1988 November 9. Received 1988 November 1; in original form 1988 April 8.

SUMMARY

A down-hole experiment was carried out in the transversely isotropic Oxford Clay outcropping in the south of England. Different moveout curves for the two shear wave types and anomalous amplitude features for the SV-wave were found in the field data. Based on velocity measurements carried out formerly at the site a model study was performed to explain the results. Phase velocity and group velocity curves computed analytically with the method of characteristics, and synthetic seismograms computed with the Alekseev–Mikhailenko method, are presented. The field experiment and the model studies demonstrate that the occurrence of cuspidal triangles in the qSV-wavefront is an essential feature of wave propagation in transversely isotropic media. Even for weak transversely isotropic media there is a focusing effect into the direction of the cusp which leads to prominent shear wave amplitudes in this direction. Furthermore, we examined the effect of numerical anisotropy which can contaminate the synthetic seismograms. Velocity errors are one order of magnitude higher for shear waves than for compressional waves and increase with increasing Poisson's ratio. It was found that the error can be restricted to less than 1 percent only if using a spatial sampling of three times higher than a value that would generally be regarded as sufficient in finite difference computations.

Key words: anisotropy, finite-difference method, shear waves, transverse isotropy

1 INTRODUCTION

Recent developments in wide angle reflection methods, offset vertical seismic profiling and the analysis of shear wave data have led to an increased awareness amongst exploration seismologists of the necessity to consider the influence of anisotropy on the properties of seismic waves. Transverse isotropy is generally regarded as the commonest form of anisotropic symmetry. It can be caused by layering as well as by intrinsic, microscopic properties of the rocks. Investigation on sediments have shown that large anisotropy effects are caused by clay (Brodov *et al.* 1984; Galperina & Galperin 1987). The percentage of clay in a sediment is correlated with the anisotropic property of the sediment, which can hence serve as a lithology indicator (Winterstein 1986).

In the past, interest in transverse isotropy has tended to focus on its influence on normal moveout velocities (Berryman 1979; Byun 1982, 1984; Helbig 1984; Krey & Helbig 1956; Levin 1979, 1980; Thomas & Lucas 1977). Only a few studies exist that investigate the wave amplitudes in transversely isotropic media (Payton 1983; Mikhailenko 1984; White 1982). However, Wright (1987) and Banik (1987) have emphasized that transverse isotropy might have a significant effect on amplitude versus offset studies.

In this paper a field experiment is described which was carried out to investigate the effects of transverse isotropy in a clay layer. A simple surface to borehole survey with a single downhole three-component geophone was performed. At the same site the elastic coefficients for the shear wave velocities have been derived (Barnes 1983) for different depths by fitting theoretical to measured phase velocity versus angle curves (White, Martineau–Nicoletis & Monash 1983). These data, together with data from a sonic log and a surface refraction survey (King 1983; King, Somerton & Davis 1982), were used to compute synthetic seismograms.

A model study was performed to simulate the field data. It included an investigation of the kinematics and dynamics of wave propagation in a weak and a strong transversely isotropic medium and the influence of the source type on the amplitudes. Analytical velocity and polarization versus angle curves are presented. Synthetic seismograms were computed using a combination of the integral transform method and a finite difference scheme (Martynov & Mikhailenko 1984).

2 DEFINITIONS AND METHODS OF COMPUTATION

Linearly elastic material is described by the generalized Hooke's law relating the stress tensor, p_{ij}, to the strain tensor e_{ij}. Due to symmetry conditions, the fourth order elasticity tensor, e_{ij}, is given by only 21 independent constants for a general anisotropic elastic medium. This number reduces to five in the case of transversely isotropic media with a vertical

axis of symmetry:

$$\begin{bmatrix} p_{11} \\ p_{22} \\ p_{33} \\ p_{23} \\ p_{31} \\ p_{12} \end{bmatrix} = \begin{bmatrix} c_{11} & c_{12} & c_{13} & & & 0 \\ c_{12} & c_{11} & c_{13} & & & \\ c_{13} & c_{13} & c_{33} & & & \\ & & & c_{44} & & \\ & & & & c_{44} & \\ 0 & & & & & \tfrac{1}{2}(c_{11}-c_{12}) \end{bmatrix} \begin{bmatrix} e_{11} \\ e_{22} \\ e_{33} \\ 2e_{23} \\ 2e_{31} \\ 2e_{12} \end{bmatrix}$$

An isotropic medium is a special case of a transversely isotropic medium with $c_{33} = c_{11} = \lambda + 2\mu$, $c_{12} = c_{13} = \lambda$, and $c_{44} = \mu$ where λ, μ are the Lamé parameters.

A major difference between wave propagation in isotropic and transversely isotropic media is that in the latter case the phase velocity curve and the wavefront are neither congruous nor circular (Fig. 1). The wave vector, **k**, is perpendicular to the wavefront and points along the phase velocity vector. However, this direction is different from the ray direction which is also termed the group velocity vector (Berryman 1979). The angles between the phase and group velocity vectors and the vertical direction are the phase angle and the group angle, respectively.

In transversely isotropic media, P-waves are not purely longitudinal and SV-waves are not purely transversal. Instead, polarization directions are deviated from the direction of propagation (**k**). Furthermore, for intermediate transmission angles, the SV-wave velocities are dependent on the P-wave velocities. In transversely isotropic media these waves are therefore referred to as quasi P- (qP) and quasi SV- (qSV) waves.

For propagation along horizontal (h) or vertical (v) directions the phase velocities are directly related to the elastic parameters. The qP-wave velocities for the waves travelling in these directions are $\alpha_h = (c_{11}/\rho)^{1/2}$ and $\alpha_v = (c_{33}/\rho)^{1/2}$. For the qSV-wave the velocity is $\beta_h^{qSV} = \beta_v^{qSV} = (c_{44}/\rho)^{1/2}$ in both directions. For SH-waves travelling in horizontal or vertical directions the velocities are $\beta_h^{qSV} = [0.5(c_{11} - c_{12})/\rho]^{1/2}$ and $\beta_v^{qSV} = (c_{44}/\rho)^{1/2}$ (ρ = density). However, the remaining parameter, c_{13}, cannot be related directly to a velocity.

One method we used to study wave propagation in transversely isotropic media was to solve the eigenvalue problem for plane wave solutions to the wave equation. This yields phase velocity and particle motion directions for plane waves incident upon the medium at different angles. Considering the propagation of waves diverging from a *point source, the resulting wavefront can be constructed by* computing the envelope of the plane waves (Huygen's method; Payton 1983). An equivalent approach is to compute the group velocity vector (Berryman 1979).

These results are valid for wave propagation in the far-field. Furthermore, they imply an explosion source for the P-SV waves and a single-force source for the SH waves. The velocity curves can be used to trace a ray through transversely isotropic, multilayered media (Byun 1984; Stöckli 1984).

Instead of ray-tracing we used a wavenumber summation method to solve the wave equation numerically and compute synthetic seismograms. The method combines a finite integral transformation with a finite difference scheme (Martynov & Mikhailenko 1984; Alekseev & Mikhailenko 1980; Korn 1987). The method yields complete seismograms which contain all wave types including converted and inhomogeneous waves. The algorithm is sketched in Appendix A for the three components of the displacement vector.

However, numerical approximations in the finite difference scheme can cause a contamination of the synthetic seismograms by grid dispersion. Grid dispersion comprises both a frequency dependence of the wave velocities (numerical dispersion) and an angle dependence of the velocities (numerical anisotropy). It was essential to examine the effect of numerical anisotropy before modelling the anisotropy of rocks. The results are given in Appendix A.

3 FIELD EXPERIMENT

The Oxford Clay is an over-consolidated Upper Jurassic formation outcropping in the south of England. It is a mainly

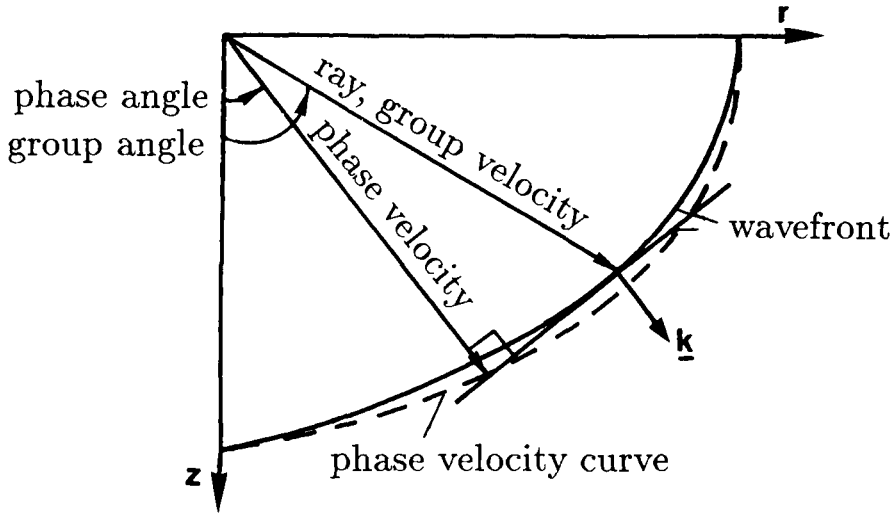

Figure 1. Wave propagation in transversely isotropic media – definitions.

homogeneous fine-grained sedimentary sequence which has been found to be transversely isotropic (King 1983). At the site near Purton/Wiltshire the sediment is about 100 m thick and overlies a limestone layer. Compressional and shear wave velocities had been measured using a variety of techniques, including down-hole and cross-hole surveys, surface refraction recordings and sonic logging (King *et al.* 1982; Barnes 1983). The velocities and elastic parameters measured in the depth range from 0 to 47 m are listed in Table 1 (values in bold print; the values in light print are referred to later in the text). Other in-hole measurements (caliper, natural gamma, density logs) had shown that, apart from two sandy intrusions at about 30 and 75 m depth, the Oxford Clay is laterally homogeneous.

Figure 2 is a sketch of the experimental geometry. Two three-component geophones were clamped in neighbouring boreholes at 38 and 45 m depth, respectively. Data were recorded for source positions in an offset range from 0 to 70 m from the wellheads, at intervals of 5 m. Different source types were used: P–SV-waves were generated using a Betsy-gun which fires a shell into the ground; SH-waves were produced by hitting the end of a plank with a sledge hammer.

The seismograms recorded in the two boreholes are shown in Fig. 3. SH-waves could only be measured in one borehole. The recorded horizontal components have been rotated into the in-line (radial) and cross-line (transversal) directions to yield maximum signal energy in the directions of P–SV- and SH-waves, respectively. All records have been normalized on a trace by trace basis.

In the vertical and radial component gathers, shear wave signals with comparable amplitudes to the P-wave signals are visible. In the vertical component gathers, qSV-waves occur at source offsets of greater than 20 m (Fig. 3a and d). Their amplitudes reach maximum values of nearly twice the qP-wave amplitude at offsets of 35 m (Fig. 3a) and 45 m (Fig. 3d). The qSV-wave arrivals in the radial component gathers (Fig. 3b and e) only exhibit large amplitudes in the offset range of 20–40 m, but can also be detected in the seismograms for smaller offsets. It is apparent from the S/N ratio that the amplitudes of the SH-waves (Fig. 3c) are approximately the same for all offsets. Note that the plank source produces a much lower frequency wavelet than the Betsy-gun. In addition to the direct waves, a small reflected signal from the clay–limestone interface is visible in Figs 3(a) and (d) at approximately 0.1 s.

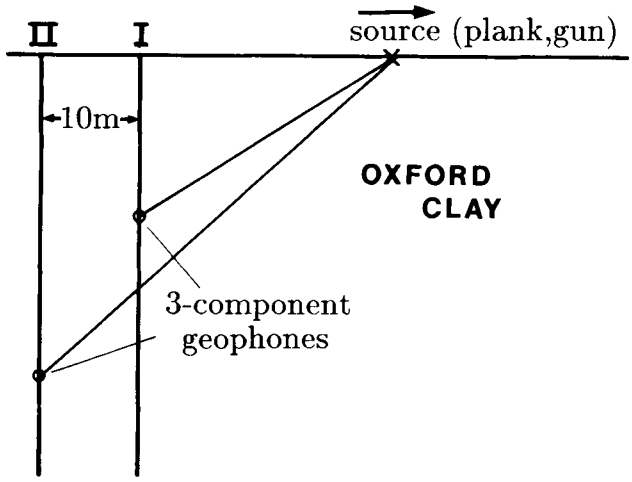

Figure 2. Sketch of the experimental geometry (I, II: boreholes).

A comparison of the moveout curves of the qSV- and SH-waves gives clear evidence of the anisotropic properties of the Oxford Clay. In addition, hodograms have been produced for the qSV-signals recorded in borehole II in the offset range 35–55 m (Fig. 3f). The polarization directions are deviated from the perpendicular to the ray directions, shown as straight lines in the figure. The influence of the vertical velocity gradient on the ray directions slightly diminishes this effect.

Our objective for the following modelling is to explain all the travel time, amplitude and polarization characteristics inherent in these field data.

Table 1. Elastic parameter for the field case ($\alpha_{h,v}$, $\beta_{h,v}$: P- and S-wave velocities for the horizontally and vertically travelling waves). Bold print: measured velocities (the P-wave velocities are mean values for a depth range obtained from a velocity log. The single velocity value for horizontally travelled P-wave is an estimate from a refraction survey. Shear-wave velocities are obtained from a downhole experiment). Light print: estimated velocities and calculated c_{13}-parameters (for the modelling, a constant density of 1.8 g cm^{-3} was assumed).

Depth range [m]	Depth [m]	α_v [km/s]	α_h [km/s]	β_v [km/s]	β_h [km/s]	c_{13} $10^{10}\frac{dyn}{cm^2}$
	0.0	1.60	1.62	**0.17**	**0.20**	4.504
	7.0	1.75	1.78	**0.20**	**0.27**	5.369
	12.0	1.75	1.78	**0.22**	**0.32**	5.332
	17.0	1.75	1.78	**0.25**	**0.36**	5.297
15.-20.	17.5	-	**1.70**	-	-	-
	22.0	1.75	1.78	**0.28**	**0.42**	5.224
	27.0	1.75	1.78	**0.33**	**0.53**	5.116
25.-30.	27.5	**1.75**	1.78	-	-	-
	32.0	1.88	1.91	**0.47**	**0.58**	5.570
30.-35.	32.5	**1.88**	1.91	-	-	-
	37.0	1.80	1.83	**0.39**	**0.59**	5.293
35.-40.	37.5	**1.80**	1.83	-	-	-
	42.0	1.80	1.83	**0.40**	**0.57**	5.256
40.-45.	42.5	**1.80**	1.83	-	-	-
	47.0	1.80	1.83	**0.39**	**0.57**	5.358

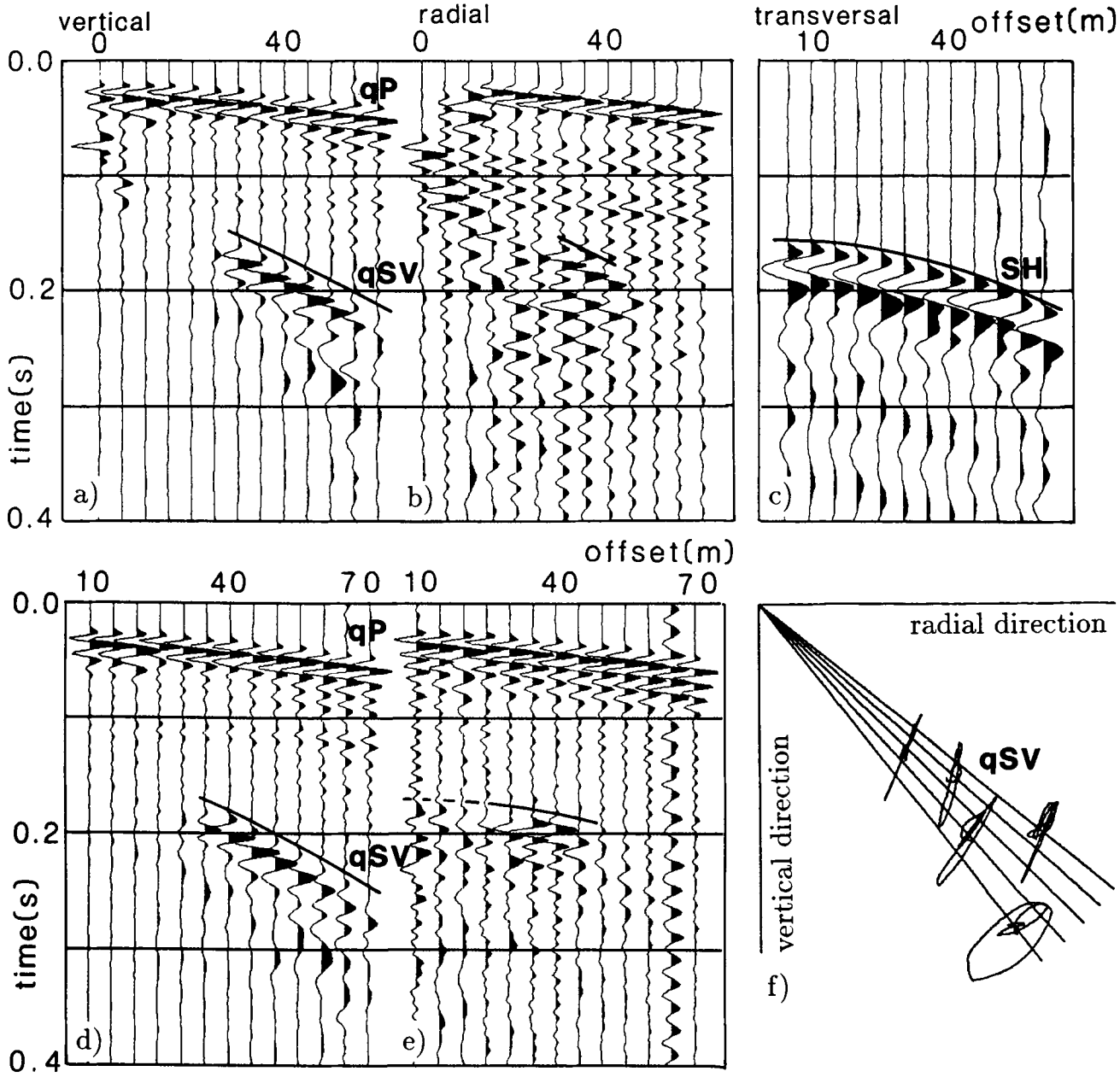

Figure 3. Field data: seismograms for different source offsets measured in borehole I (a–c) and borehole II (d, e) using different sources for the qP–qSV- and SH-wave generation, respectively. In (f) hodograms computed from the qSV-wave signals are depicted.

4 MODEL STUDIES

4.1 General remarks

Inspection of Table 1 (bold print) shows that shear wave velocities have been measured over the whole depth range. Also P-wave velocities for the vertically travelling waves are given in the depth range from 25 to 45 m. However, no values are available for the P-wave velocity in the shallower parts of the sediment and only one velocity value for the horizontally travelling P-wave is given. Thus, the measurements provide only a rough estimate of the P-wave anisotropy and furthermore no c_{13}-parameters have been determined. Preliminary studies were therefore necessary to estimate these parameters.

To achieve this, a general investigation of the dynamic and kinematic characteristics of wave propagation in transversely isotropic media was carried out. The results are described in the first part of this section. The elastic parameters were chosen to model the extreme cases of strong and weak transverse isotropy within the range of parameters for measured anisotropy as compiled by Thomsen (1986). Based on these studies, the P-wave anisotropy and c_{13}-parameters for the field case modelling were estimated by a trial and error procedure. These parameters were constrained principally by the travel times of the qSV-wave signals in the data which could be computed analytically for vertically homogeneous models. In the second part of this section, the simulation results for the final model derived for the field case are presented.

Poisson's ratio for the Oxford Clay is about 0.47. Unfortunately, velocity errors due to numerical anisotropy were found to be unacceptably large for high Poisson's ratios (Appendix A). However, significant errors in the

Table 2. Elastic parameter for three models (the anisotropy factors $\epsilon^{qP,qSV,SH}$ are defined as in Banik (1987)).

Model	c_{11}	c_{33}	c_{13} $10^{10}\frac{dyn}{cm^2}$	c_{44}	c_{12}	ρ $\frac{g}{cm^3}$	ϵ^{qP}	ϵ^{qSV}	ϵ^{SH}
strong transverse isotropy	14.82	12.21	6.70	1.31	6.11	1.00	0.10	0.61	0.82
weak transverse isotropy	9.24	9.00	5.04	1.22	4.15	1.00	-0.04	0.22	0.30
clay	6.028	5.832	5.607	0.113	5.299	1.80	0.02	0.20	0.80

modelling of the field data could be prevented by increasing the number of grid points per wavelength. This number was three times as high as the value that would generally be regarded as sufficient sampling in finite difference computations.

The models investigated in the following general study represent unbounded media, consequently the results do not contain effects caused by the free surface or by artificial boundaries. To model the field case a free surface was introduced.

4.2 Strong and weak transverse isotropy – general study

The elastic parameters for the two transversely isotropic media which we consider are given in Table 2. Note that the anisotropy factors (Banik 1987) are more than twice as high for the 'strong transversely isotropic' medium than for the 'weak transversely isotropic' medium.

Figures 4 and 5 show the analytically computed velocity and polarization curves for both media for a range of angles from 0° (vertical direction) to 90° (horizontal direction). The phase velocity curves for the weakly anisotropic medium (Fig. 4a) are flatter with less pronounced velocity differences than for the strongly anisotropic medium (Fig. 5a). The phase velocities of the horizontally travelling qP-wave and SH-wave are higher than the velocities for these waves travelling in the vertical direction. In contrast, the qSV-wave velocities in horizontal and vertical direction are identical and are equal to the SH-wave velocity in the vertical direction. Therefore shear-wave splitting in transversely isotropic media cannot be observed in zero-offset VSP records. However, in strongly anisotropic media qSV-wave phase velocities are distinctly different from the SH-wave phase velocities for nearly the whole range of angles of incidence.

The value of c_{13} has a significant influence on the shape of the qSV-wave phase velocity curve. If $c_{44} < c_{13} \leq (c_{33}-2c_{44})$, as is the case for both media, the curve exhibits a maximum at 45° and minima at 0° and 90°. The closer c_{13} is to c_{44} the higher is the maximum. If $c_{33} > c_{13} > (c_{33}-2c_{44})$ a minimum occurs at 45° and maxima at 0° and 90°. The maxima become higher with increasing c_{13}, c_{33} and c_{44} are the threshold values limiting the range for which real-valued solutions for every angle are obtained.

The inflections in the qSV-phase velocity curve lead to cuspidal triangles in the respective group velocity curve or wavefront. It means that two or three qSV-wave signals exist in the directions of the cusps. c_{13} was chosen such that the qSV-wave cusp is pronounced in the data for the strongly anisotropic medium (Fig. 5b) and is just recognizable in the data for the weakly anisotropic medium (Fig. 4b).

The polarization of the qP- and qSV-wave is shown in two different ways: the deviation of the polarization directions from the wave vector direction and its perpendicular is shown in Figs 4(c) and 5(c). The absolute values of the polarization angles are the same for qP- and qSV-waves because their polarization directions are perpendicular to each other. They reach a maximum of 8.5° in the case of the strongly anisotropic medium and a maximum of 3.5° in the case of the weakly anisotropic medium.

However, it is more interesting to visualize the polarization with respect to the group velocity direction or ray direction (Figs 4d and 5d), because these polarization angles can also be obtained from hodogram analyses of seismograms. The curves for the qSV-wave are multivalued, as are the group velocity curves. The values at a group angle of 40° in Fig. 5(d), for example, means that one qSV-phase is polarized perpendicular to the ray direction (polarization angle = 0°) and that the two other phases are polarized in the directions +35° and −42° with respect to the perpendicular to the ray direction. The maximum deviations from the perpendicular to the ray direction are about 25° and 50°, respectively, for the two media. These significant values suggest that the polarization direction of the qSV-wave with respect to the ray direction can be used as diagnostic of transversely isotropic media.

Figures 6 and 7 show the seismogram gathers for the three displacement components. P-waves were initiated by an explosion point-source and SH-waves by a horizontal single force point-source. The seismograms were computed for a circular profile with the source-point at the origin and a radius of 100 m.

The qP-, qSV- and SH-wave signals in the seismograms align along wavefronts which fit the analytical curves (dashed lines). But qSV-phases are recognizable also beyond the tips of the cusps (examples marked by arrows). White (1982) interpreted these phases as near-field effects. He showed that their amplitudes decrease more rapidly with distance from the source than the amplitudes of the analytically predicted signal phases.

The synthetic seismograms provide additional information about the amplitudes of the signal phases. In the case of the strongly anisotropic medium, the branch of the qSV-wavefront with decreasing group velocities is prominent in the angle range from 25° to 90° (Fig. 7, radial cpt). The amplitudes are high, especially close to the cusp tip at 25°. In the case of the weakly anisotropic medium the largest qSV-wave amplitudes occur for phases in the angular range close to 45°, where the cusp lies (Fig. 6). Transverse isotropy also leads to an angular dependence of the SH-wave amplitudes. For the strongly anisotropic medium the amplitude of a wave travelling in the horizontal direction is about 60 per cent higher than the amplitude of the vertically travelling wave.

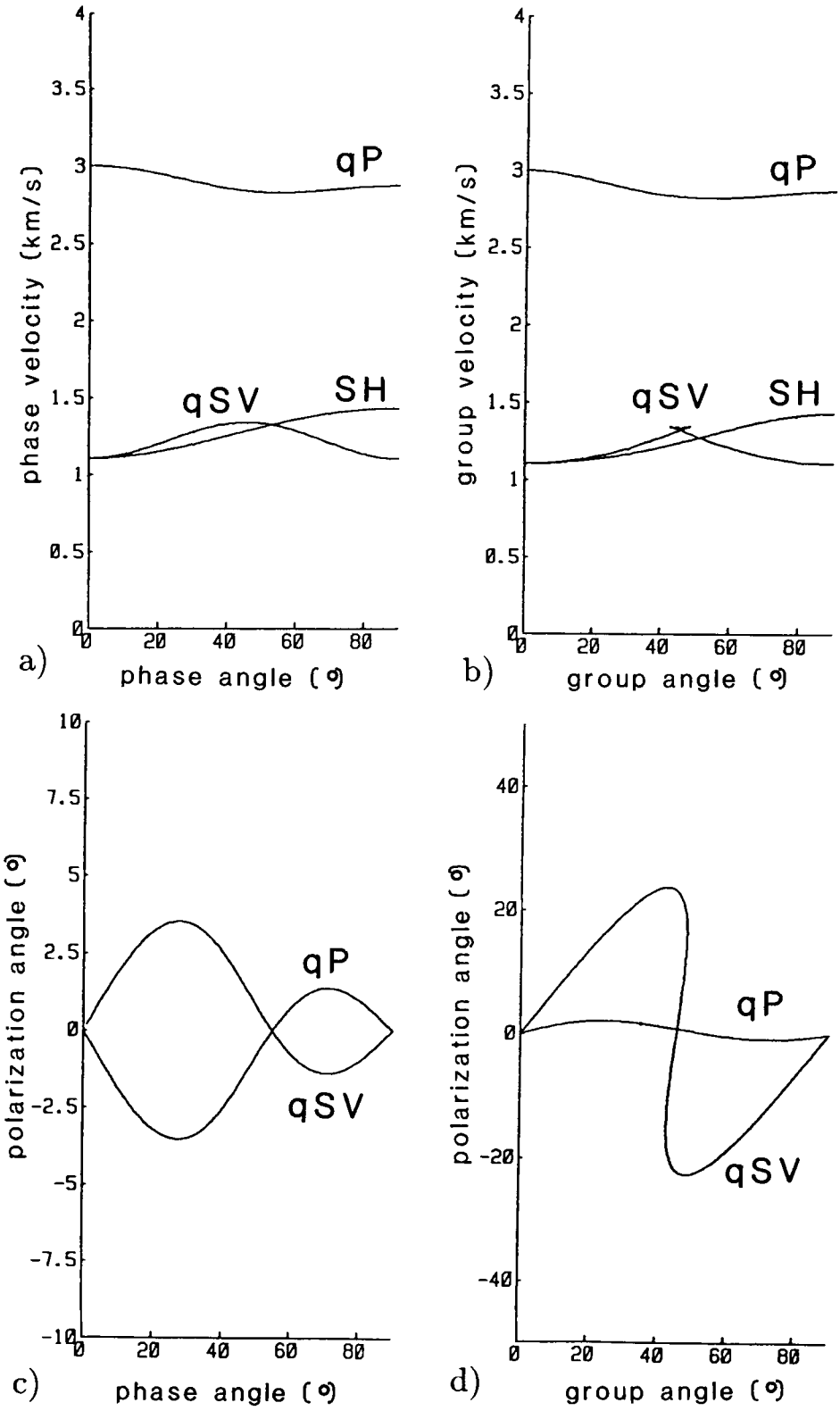

Figure 4. Weak transverse isotropy: phase- (a) and group- (b) velocity curves and polarization curves. In (c) is represented the polarization angles relative to the direction of propagation (qP) or its perpendicular (qSV) and in (d) the polarization angles relative to the ray direction (qP) or its perpendicular (qSV).

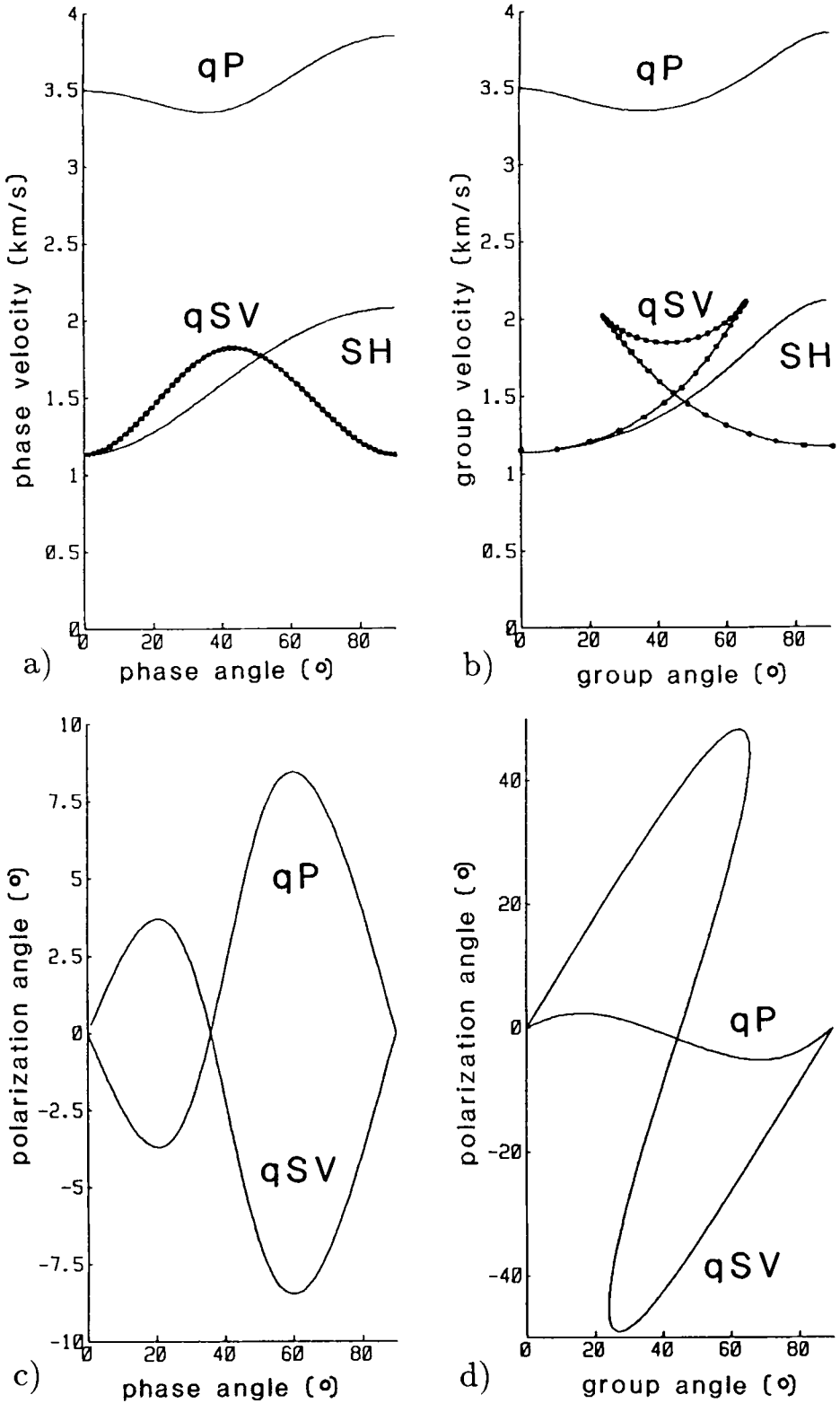

Figure 5. Strong transverse isotropy: phase- (a) and group- (b) velocity curves and polarization curves (c, d; see caption of Fig. 4).

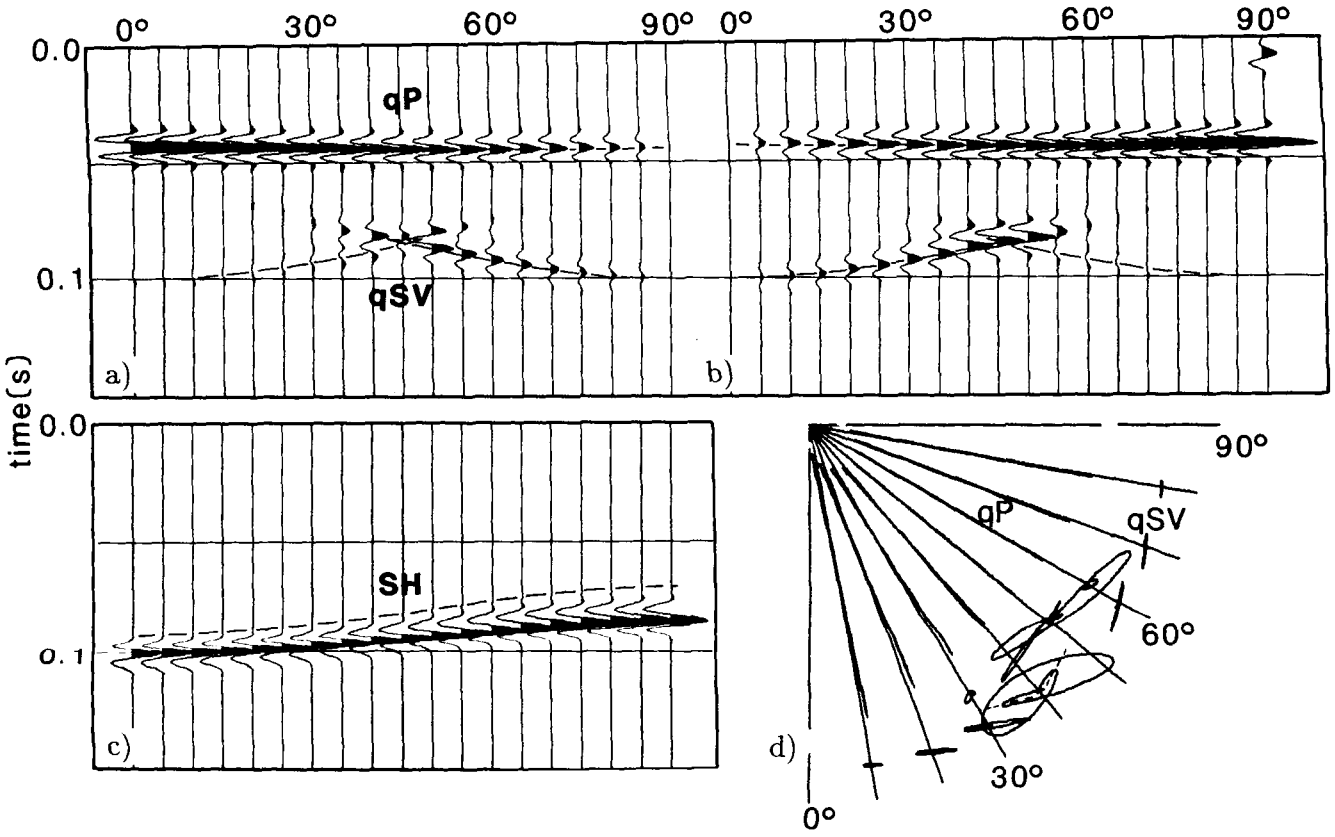

Figure 6. Weak transverse isotropy: Seismograms computed for a circular profile. (a, b) Vertical and radial component gathers with qP- and qSV-wave signals. (c) Transversal component gather with SH-wave signals. (d) Hodograms with qP- and qSV-wave particle motion at different ray angles.

Also depicted in Figs 6 and 7 are particle motion diagrams or hodograms for the qP- and qSV-waves. Here, it can be seen that the qP-wave amplitude is dependent on angle: for both media, amplitude minima occur in the angular range from 30° to 60°. In the case of the strongly anisotropic medium the variation can be as large as 50 per cent of the maximum amplitude.

The polarization directions of the qP-wave are nearly parallel to the ray directions for all angles. The deviations which are visible are identical to the polarization angles computed analytically with respect to the ray directions (Figs 4d and 5d). Naturally, the polarization of the qSV-wave signals also agree with the analytical results. In Fig. 7, for example, the two qSV hodograms at 40° indicate three different polarization directions. One direction is perpendicular to the ray direction, and corresponds to the value 0° in the analytical curve (Fig. 5d). This hodogram is of the qSV signal at the front branch of the cusp (Fig. 5b). The two other directions visible in the second hodogram belong to the qSV-wave signals of the decaying branches of the cusp. The polarization directions of these phases which are nearly perpendicular to each other can be more clearly distinguished in the two hodograms at 60°, for example.

For the weakly anisotropic medium, the qSV-wave is characterized by elliptical polarization in the range of angles enclosing the cusp (Fig. 6). This is due to superposition of qSV-phases whose polarization directions can be distinguished at the beginning and the end of the hodograms.

Figures 8 and 9 illustrate the influence of a different source type on the amplitudes. The seismograms were computed for a vertical single force source. If inserted into a homogeneous (isotropic) medium, this source radiates compressional waves with maximum amplitudes in the vertical directions and shear waves with maximum amplitudes in the horizontal directions. The maximum shear wave amplitude is a factor α^2/β^2 (α, β; P- and SV-wave velocities) higher than the maximum amplitude of the compressional wave.

Due to these specific radiation features of the source, qP-wave amplitudes in the seismograms are significantly lower than the qSV-wave amplitudes. In both media the qSV-waves associated with the front branches of the cusps exhibit high amplitudes in the radial component records. In the vertical component records the qSV-wave signals with large amplitudes are associated with the wavefront branches with decreasing velocities for increasing angles.

The differences in amplitudes for the different branches of the qSV-wave, the radiation of qSV-waves from an explosion source, and the dependence of amplitudes on the transmission angle are all features of wave propagation in a transversely isotropic medium. Levin (1979) assumed that the density of velocity values on the wavefront curve is an indication of the amplitude of the wave. (For demonstration, the group- and phase-velocity values computed for the qSV-wave are marked by symbols in Fig. 5.) This should determine the gross amplitude features, because the density

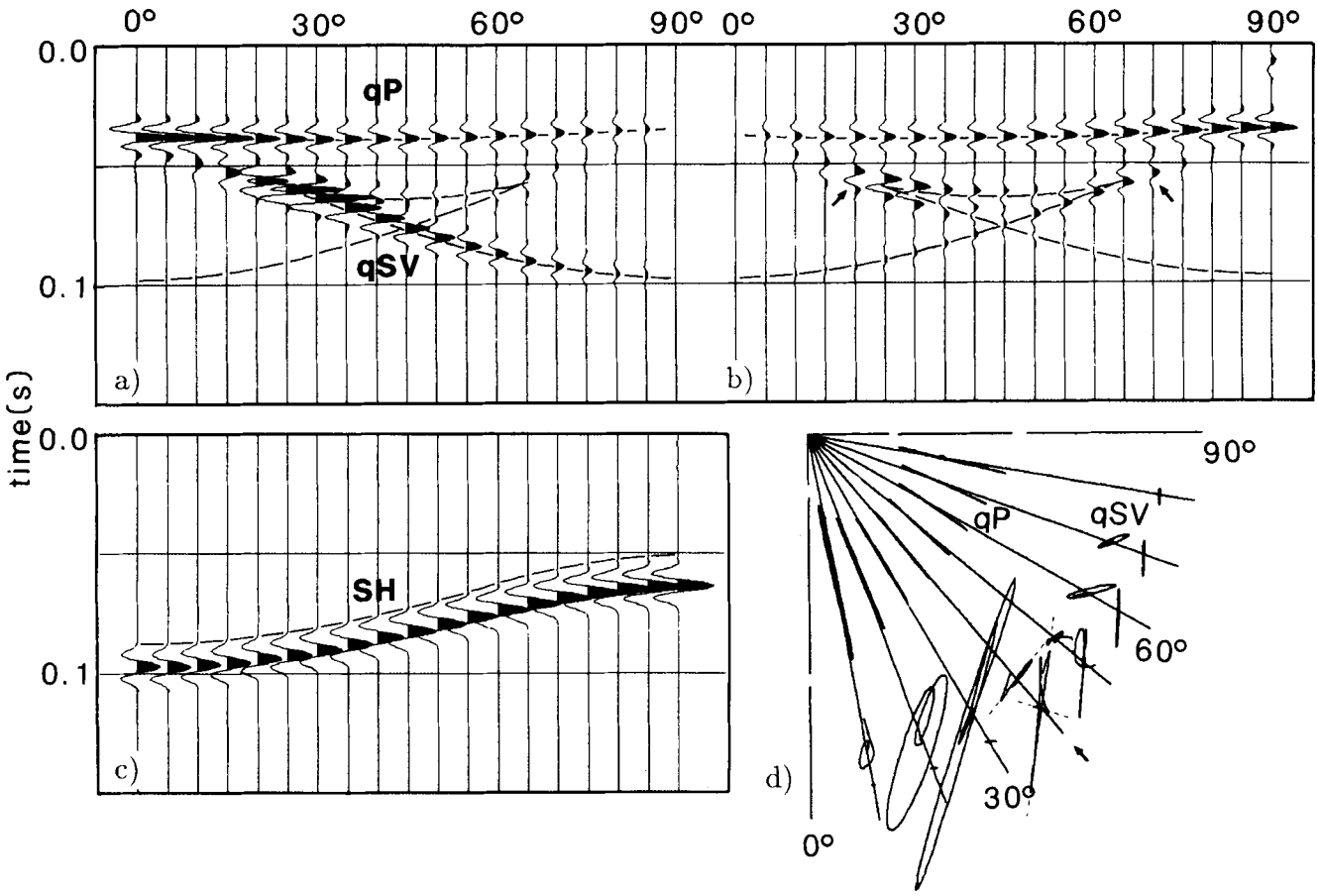

Figure 7. Strong transverse isotropy: seismograms computed for a circular profile. (a)–(d) as in Fig. 6.

of velocity points is identical to the density of plane waves of equal amplitude (cf. the coverage in ray tracing). The model studies confirm that qSV signals associated with the cusp, especially those at the tips of the cusp, exhibit prominent amplitudes in the seismogram. These parts of the wavefront are built up by a larger number of superposing plane waves than other parts of the wavefront.

However, the different signal amplitudes for the two side branches of the qSV-wavefront cannot be explained by different densities of plane waves. This feature becomes comprehensible by regarding wave propagation in a finely stratified medium which is analogous to a homogeneous transversely isotropic medium (Postma 1955). It can be shown that the two side branches of the qSV-wavefront are made up by plane waves with angles of incidence below the first and above the second point of inflection in the phase-velocity curve, respectively. Hence, the low signal amplitudes for one of the branches can be related to the low

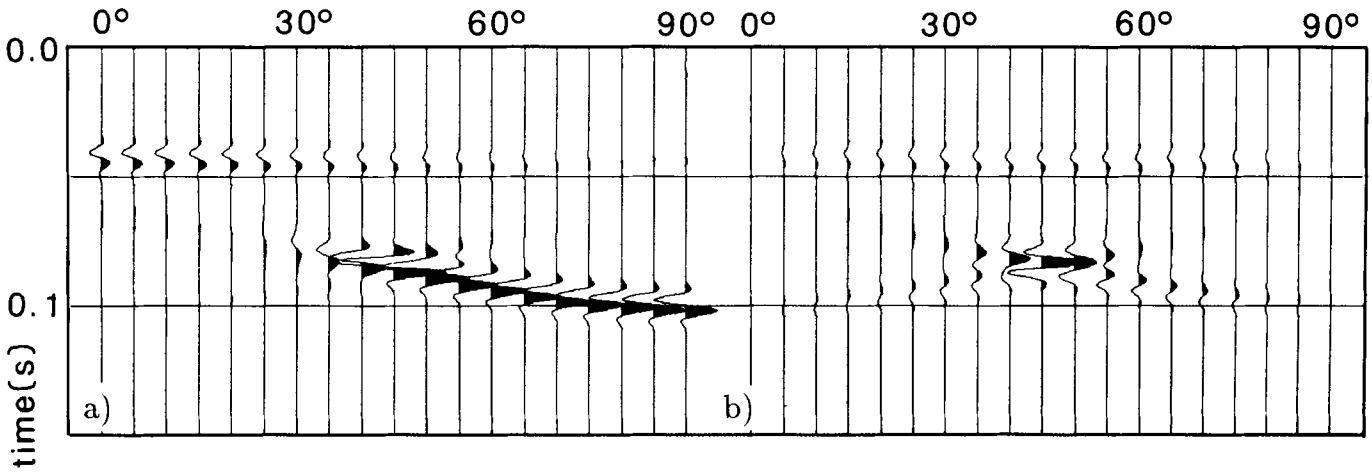

Figure 8. Weak transverse isotropy: influence of a vertical single-force on the amplitudes. (a) Vertical component, (b) radial component.

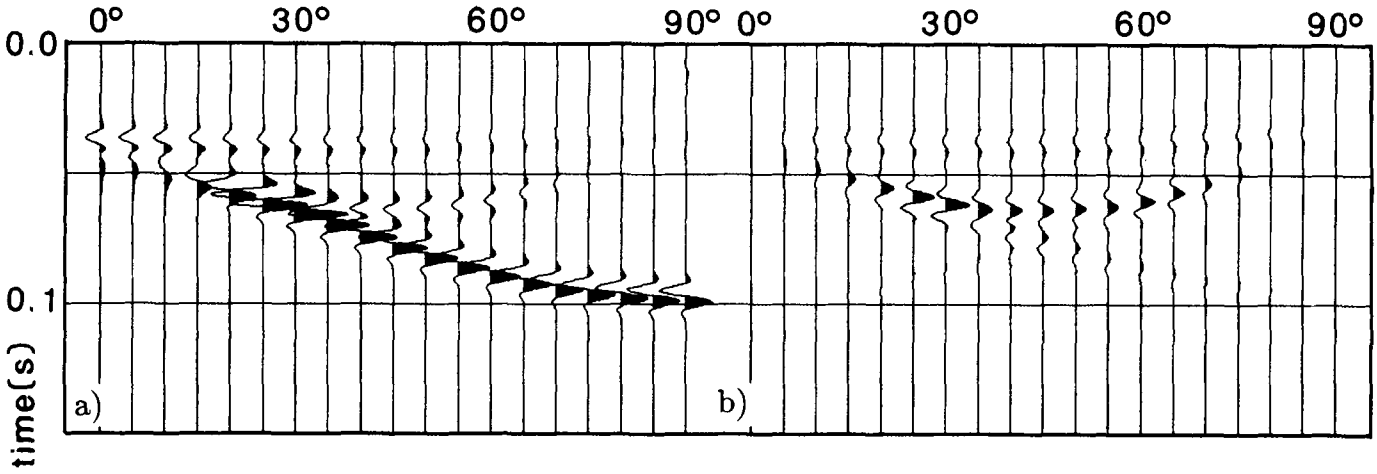

Figure 9. Strong transverse isotropy: influence of a vertical single-force on the amplitudes. (a) Vertical component, (b) radial component.

transmission amplitudes for P to SV converted waves in stratified media if the angles of incidence are steep. Furthermore, the shear wave generation by an explosion source is explained by conversion.

4.3 Modelling of the field case

The field data and the synthetic data for the weak transversely isotropic medium resemble one another in the occurrence of a single qSV-wave signal and the amplitude characteristics of the qSV-wave. This suggests the existence of a small cusp at 45°. By trial and error it was found that the best fit to the field data was obtained if c_{13} was chosen to be $c_{13}=(c_{33}-2c_{44})$; in addition, the velocity of the horizontally travelling qP-wave was assumed to be 1.5 per cent higher than the velocity for qP-waves travelling in the vertical direction. Both choices mean that the medium is nearly isotropic for P-waves. All elastic parameters used for the modelling of the field case are given in Table 1 (light and bold print). These parameters were assumed to change gradually between the samples. A vertical and a horizontal single-force source was applied to the free surface to generate qP–qSV-waves and SH-waves, respectively. In contrast to a single force in an unbounded medium the vertical single force positioned at the free surface radiates a maximum of shear wave energy at about 45°.

The effect of the velocity gradient and the influence of the radiation pattern of the source at the surface on the qP-qSV-wave seismograms are shown in Fig. 10. In Figs 10(c) and (d) the radial and vertical components of the displacement vector computed for the gradient model on a circular profile with a radius of 40 m are depicted. For comparison, the seismograms in Figs 10(a) and (b) have been computed for a homogeneous, transversely isotropic medium with a set of intermediate values for the elastic parameters (Table 2).

The seismograms for both models (Figs 10a–d) show that P-wave signals with only very small amplitudes compared with the amplitudes of the shear waves are radiated by the source. This is due to the extremely high Poisson's ratios in these models. Although the choice of the elastic parameters means that P-wave anisotropy is very small, the anisotropy effect on the qSV-wave is significant. The existence of a small cusp in the group velocity curve causes a focusing of wave energy in the direction of the cusp. As shown in Figs 10(a) and (b) this leads to similar amplitude characteristics in the seismograms computed for the homogeneous medium as those depicted in Fig. 8. However, the influence of the free surface on the radiation pattern causes a further concentration of shear wave energy for waves propagating in the directions around 45°.

A velocity gradient can counteract such an accumulation of wave energy as the comparison with the seismograms in Figs 10(c) and (d) shows. However, in the angular range from 45° to 50° the amplitudes in the seismograms for both components are still significantly higher than for other transmission angles. Furthermore, a rather abrupt increase in amplitude between 40° and 45° is visible. That these amplitude characteristics are mainly due to transverse isotropy and not altogether an effect of the radiation pattern was tested by comparison with results obtained for an isotropic gradient model for which the velocities of the vertically travelling qP- and qSV-waves (Table 1) were taken. In the case of isotropy the amplitudes increase smoothly with increasing angles in the range from 0° to 45° (no picture).

With the source–receiver configuration used in the field experiment, waves transmitted through the media in the angular range from 0° to 60° were measured. Fig. 10 shows that this is the range where the influence of cusping is the strongest visible in the data, as discussed before. Note that the data in this angular range do not contain surface waves which exhibit large amplitudes in the seismograms recorded at the surface or close to it (Fig. 10: 80°–90°).

Figure 11 shows the synthetic seismogram gathers for the same source–receiver configuration as in the field experiment and for all three components. A close inspection of the travel times for both shear wave types in the synthetic seismograms indicates that the kinematics of the shear waves are quantitatively predicted by the model. The moveout curves of the recorded signals, which are drawn on the seismogram gathers, fit nearly perfectly. Also the dynamics in the field seismograms (Fig. 3) and the synthetic

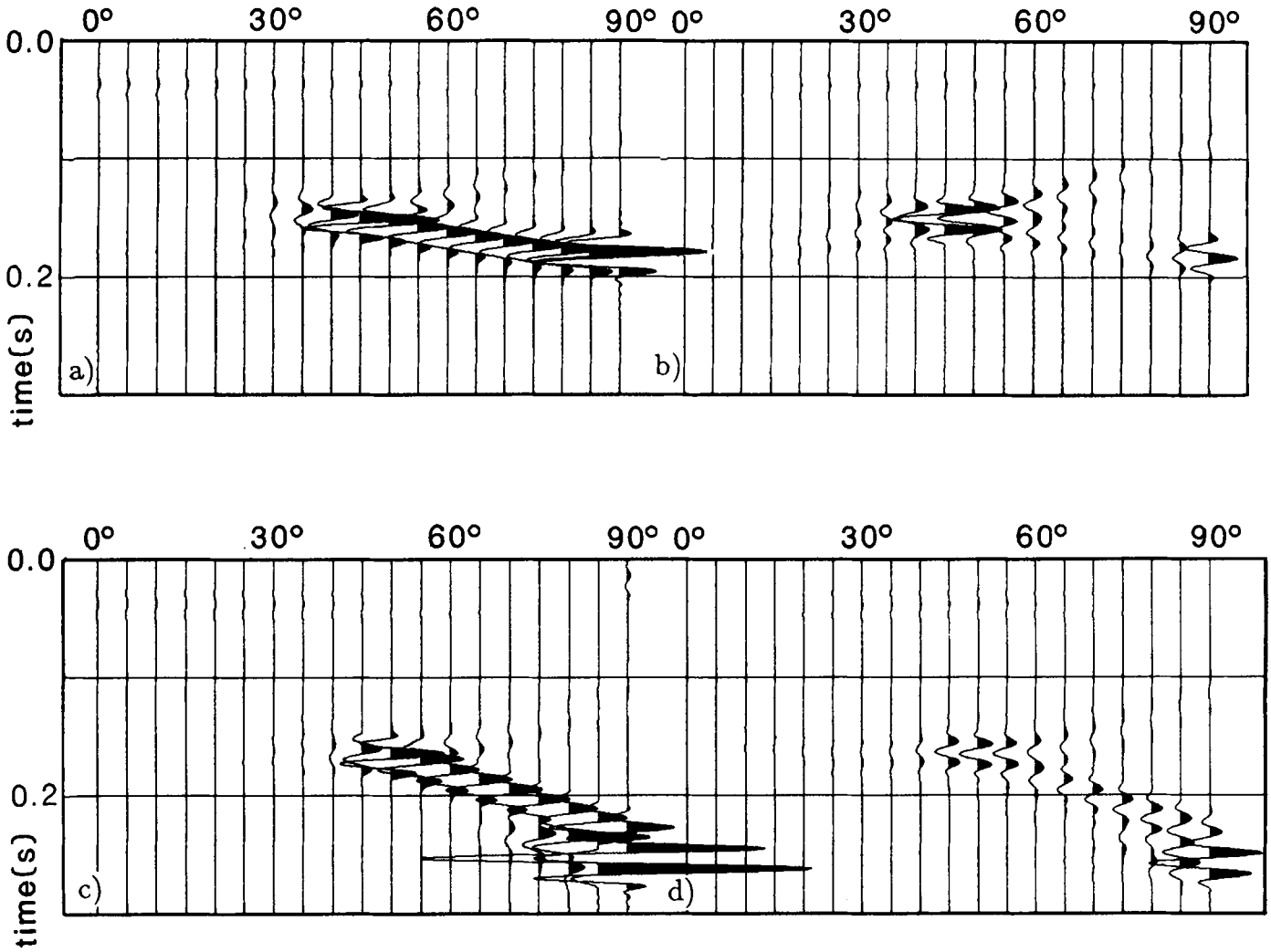

Figure 10. Synthetic data from the field case modelling: seismograms computed for a circular profile. (a, b) Vertical and radial component gathers computed for the homogeneous model of the Oxford clay layer. (c, d) Vertical and radial component gathers computed for the gradient model of the Oxford clay layer.

seismograms (Fig. 11) are—at least qualitatively—in agreement. An abrupt increase in the amplitude of the qSV-signal occurs at offsets between 30 and 35 m (Fig. 11a) or 35 and 40 m (Fig. 11d) in the vertical component gathers. In both vertical and radial component gathers, the amplitudes of the qSV-signals reach a maximum at larger offsets.

Two differences between the synthetic data (Fig. 11) and the field data (Fig. 3) are visible. Firstly, the amplitudes of the qP-wave signals compared with the amplitudes of the qSV-wave signals are much higher in the field data than in the synthetic data. Furthermore, in the field data the decrease with offset of the shear wave amplitudes is more distinct than in the synthetic data. Both effects may be explained by absorption. It can be estimated from a comparison of relative amplitudes that the absorption for the shear wave is at least one order of magnitude higher than the absorption for the compressional wave. A further imperfection of the model is indicated by the differences in the polarization directions of the qSV-waves in the field seismograms and in the synthetic seismograms.

5 CONCLUSION AND DISCUSSION

The field experiment and the model studies presented in this paper demonstrate the significant differences in wave propagation between transversely isotropic media and isotropic media. In particular, the occurrence of cuspidal triangles in the qSV-wavefront is an essential feature. In the case of strong transverse isotropy, large cusps might exist which mean that up to three qSV-wave signals can occur in the seismograms. Their group velocities can be larger than the maximum SH-wave velocity. In the case of weak transverse isotropy, even very small cusps have a significant effect on the amplitude of the qSV-wave.

The field data is an example of wave propagation in a weak transversely isotropic medium. The different moveout curves for qSV- and SH-waves indicate the anisotropy of the clay layer. They have been modelled quantitatively using a model with gradually increasing velocities which was derived from velocity recordings. Furthermore, the amplitude features of the qSV-wave appear also to be a significant indicator of transverse isotropy. Significant qSV-wave

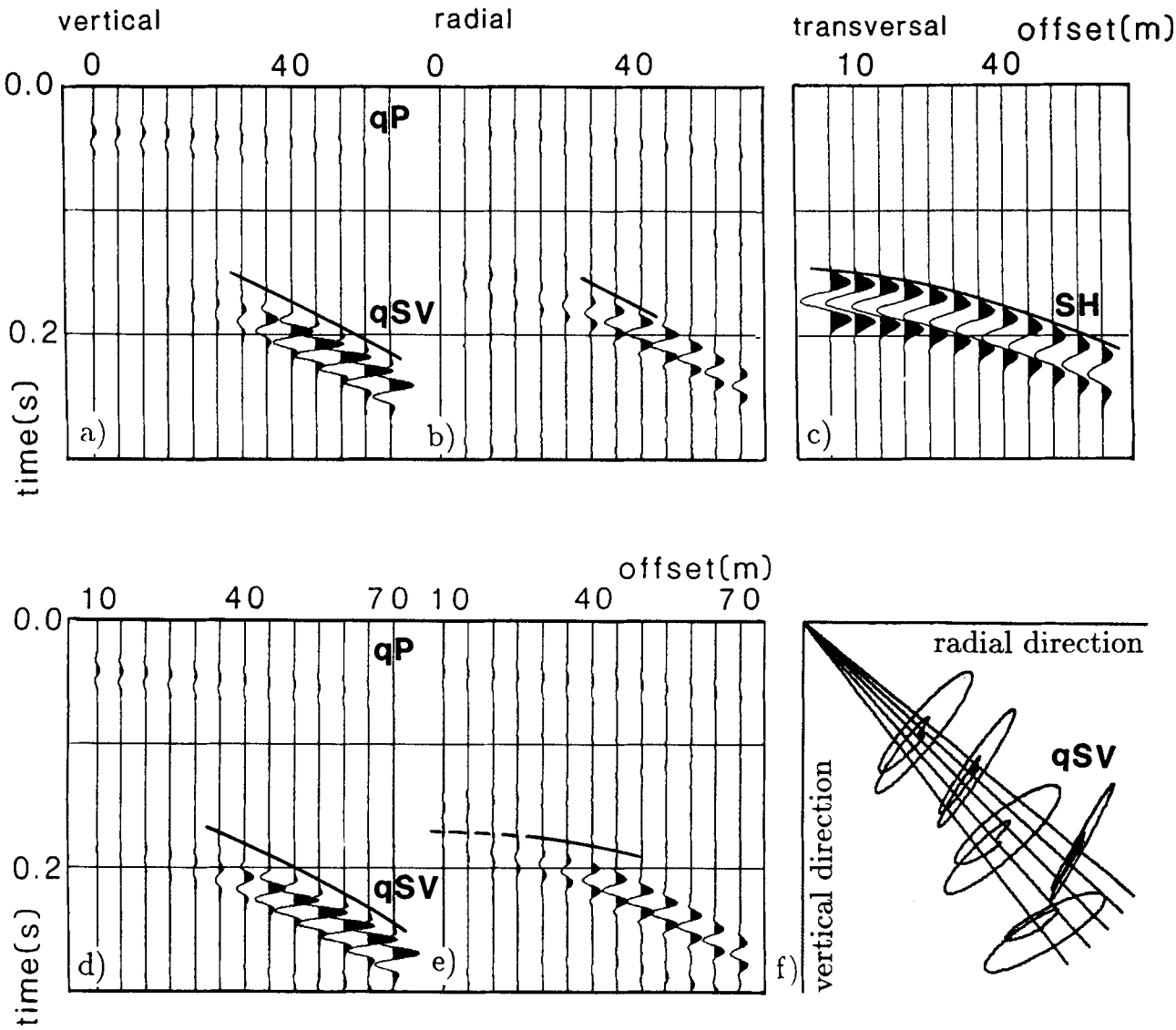

Figure 11. Synthetic data from the field case modelling. (a–c) Vertical, radial and transversal component gathers computed for borehole I. (d, e) Vertical and radial component gathers computed for borehole II. (f) Hodograms computed from the qSV-wave signals in Fig. 11(d) and (e).

amplitudes were restricted to an offset range which corresponds to transmission angles of about 45°. The model studies have shown that this can be explained by a focusing effect in the direction of the cusp, which is inherent in wave propagation in transversely isotropic media. The focusing effect can be diminished by a velocity gradient. The amplitude features of the recorded qSV-wave were qualitatively simulated in the synthetic data.

Levin (1979) has published an example that shows the effect of strong transverse isotropy in field data: an anomalous crossing of the moveout curves for qSV- and SH-waves was explained by the qSV-wave group velocities being higher than the SH-wave velocities of signals associated with the front branch of the cusp. However, only a single qSV-wave phase was recognized which Levin (1979) attributed to the waves belonging to the other branches of the wavefront possibly having only small amplitudes. The model studies presented here confirm those amplitude characteristics. qSV-signals associated with the cusp, especially those at the tips of the cusp, exhibit prominent amplitudes in the seismograms. White (1982) has shown that a further feature of these qSV-phases is that the amplitude decreases with distance by less than the geometrical spreading factor.

Reflection amplitudes from interfaces between isotropic and transversely isotropic media have been investigated by Wright (1987) and Banik (1987). The studies presented here have shown that the amplitudes of qP-, qSV- and SH-waves can exhibit significant variations with angle also for transmission through a transversely isotropic layer. This influences the overall amplitudes of the waves. In the interpretation of amplitude variation with offset experiments it is therefore essential that the effects of transverse isotropy on transmission as well as reflection are taken into account.

ACKNOWLEDGEMENTS

We thank Dr Michael Korn for providing his Alekseev–Mikhailenko programs which were extended to include transverse isotropy. We are grateful to Gerhard Pratt and Dr Anna Thomas-Betts for helpful discussions and carefully reading the manuscript. Furthermore, we thank BP for the financial support.

REFERENCES

Alford, R. M., Kelly, K. R. & Boore, D. M., 1974. Accuracy of finite-difference modelling of the acoustic wave equation, *Geophysics*, **39**, 834–842.

Alekseev, A. S. & Mikhailenko, B. G., 1980. The solution of dynamic problems of elastic wave propagation in inhomogeneous media by a combination of partial separation of variables and finite-difference methods, *J. Geophys.*, **48**, 161–172.

Alterman, Z. S. & Aboudi, J., 1970. Source of finite extent, applied force and couple in an elastic half-space, *Geophys. J. R. astr. Soc.*, **21**, 47–64.

Banik, N. C., 1987. An effective anisotropy parameter in transversely isotropic media, *Geophysics*, **52**, 1654–1664.

Barnes, S. R., 1983. Seismic anisotropy in the Oxford Clay at Purton, near Swindon, *MSc thesis*, University of Birmingham.

Berryman, J. G., 1979. Long-wave elastic anisotropy in transversely isotropic media, *Geophysics*, **44**, 896–917.

Brodov, L. Y., Evstifeyev, V. I., Karus, E. V. & Kulichikhina, T. N., 1984. Some results of the experimental study of seismic anisotropy of sedimentary rocks using different types of waves, *Geophys. J. R. astr. Soc.*, **76**, 191–200.

Byun, B. S., 1982. Seismic parameters for media with elliptical velocity dependencies, *Geophysics*, **47**, 1621–1626.

Byun, B. S., 1984. Seismic parameters for transversely isotropic media, *Geophysics*, **49**, 1906–1914.

Crampin, S., 1986. Anisotropy and transverse isotropy, *Geophys. Prospect*, **34**, 94–99.

Galperina, R. M. & Galperin, E. I., 1987. An experimental study of transverse waves from shots in anisotropic media, *Geophys. J. R. astr. Soc.*, **91**, 517–533.

Helbig, K., 1984. Transverse isotropy in exploration seismics, *Geophys. J. R. astr. Soc.*, **76**, 79–88.

Kerner, C., 1989. Modelling of soft sediments and liquid–solid interfaces: modified wave number summation method and application, *Geophys. Prospect.*, submitted.

King, R. F., 1983. Seismic anisotropy in the Oxford Clay at Purton/Swindon, *Internal Report*, University of Birmingham.

King, R. F., Somerton, I. W. & Davis, A., 1982. Seismic anisotropy in the Oxford Clay at Purton/Swindon, *Internal Report*, University of Birmingham.

Korn, M., 1985. Kombination von Integraltransformationen und Finiten-Differenzen-Methoden zur Berechnung der Wellenausbreitung in geschichteten Medien, *PhD thesis*, Johann Wolfgang Goethe Universität, Frankfurt.

Korn, M., 1987. Computation of wavefields in vertically inhomogeneous media by a frequency domain finite-difference method and application to wave propagation in earth models with random velocity and density perturbations, *Geophys. J. R. astr. Soc.*, **88**, 345–377.

Krey, Th. & Helbig, K., 1956. A theorem concerning anisotropy of stratified media and its significance for reflection seismics, *Geophys. Prospect*, **4**, 294–302.

Küpper, F. J., 1958. Theoretische Untersuchungen über die Mehrfachaufstellung von Geophonen, *Geophys. Prospect*, **6**, 194–256.

Levin, K. F., 1979. Seismic velocities in transversely isotropic media, *Geophysics*, **44**, 918–936.

Levin, K. F., 1980. Seismic velocities in transversely isotropic media, II, *Geophysics*, **45**, 3–17.

Marfurt, K. J., 1984. Accuracy of finite-difference and finite-element modelling of the scalar and elastic wave equations, *Geophysics*, **49**, 533–549.

Martynov, V. N. & Mikhailenko, B. G., 1984. Numerical modelling of propagation of elastic waves in anisotropic inhomogeneous media for the half-space and the sphere, *Geophys. J. R. astr. Soc.*, **76**, 53–63.

Mikhailenko, B. G., 1984. Numerical experiment in seismic investigations, *J. Geophys.*, **58**, 101–124.

Payton, R. G., 1983. *Elastic Wave Propagation in Transversely Isotropic Media*, Nijhoff, The Hague.

Peacock, S. & Crampin, S., 1985. Shear-wave vibrator signals in transversely isotropic shale, *Geophysics*, **50**, 1285–1293.

Postma, G. W., 1955. Wave propagation in a stratified medium, *Geophysics*, **20**, 780–806.

Stöckli, R. F., 1984. Two-point ray tracing in a three-dimensional medium consisting of homogeneous nonisotropic layers separated by plane interfaces, *Geophysics*, **49**, 767–770.

Thomas, J. H. & Lucas, A. L., 1977. The effects of velocity anisotropy on stacking velocities and time-to-depth conversion, Paper presented at the meeting of EAEG, Zagreb.

Thomsen, L., 1986. Weak elastic anisotropy, *Geophysics*, **51**, 1954–1966.

Virieux, J., 1986. P–SV wave propagation in heterogeneous media: Velocity–stress finite-difference method, *Geophysics*, **51**, 889–901.

White, J. E., 1982. Computed waveforms in transversely isotropic media, *Geophysics*, **47**, 771–783.

White, J. E., Martineau-Nicoletis, L. & Monash, C., 1983. Measured anisotropy in Pierre Shale, *Geophys. Prospect*, **31**, 709–725.

Winterstein, D. F., 1986. Anisotropy effects in P-wave and SH-wave stacking velocities contain information on lithology, *Geophysics*, **51**, 661–672.

Wright, J., 1987. The effects of transverse isotropy on reflection amplitude versus offset, *Geophysics*, **52**, 564–567.

APPENDIX A

The Alekseev–Mikhailenko method and numerical anisotropy

Assuming cylindrical symmetry the equations of motion for the components U_r, U_z, U_φ of the displacement vector in the vertical heterogeneous, transversely isotropic medium are

$$\rho\frac{\partial^2 U_r}{\partial t^2}=c_{11}\left(\frac{\partial^2 U_r}{\partial r^2}+\frac{1}{r}\frac{\partial U_r}{\partial r}-\frac{U_r}{r^2}\right)+c_{13}\frac{\partial^2 U_z}{\partial z\,\partial r}+\frac{\partial}{\partial z}\left[c_{44}\left(\frac{\partial U_r}{\partial z}+\frac{\partial U_z}{\partial r}\right)\right]+F_r$$

$$\rho\frac{\partial^2 U_z}{\partial t^2}=c_{44}\left[\frac{\partial}{\partial r}\left(\frac{\partial U_r}{\partial z}+\frac{\partial U_z}{\partial r}\right)+\frac{1}{r}\left(\frac{\partial U_r}{\partial z}+\frac{\partial U_z}{\partial r}\right)\right]+\frac{\partial}{\partial z}\left[c_{13}\left(\frac{\partial U_r}{\partial r}+\frac{U_r}{r}\right)+c_{33}\frac{\partial U_z}{\partial z}\right]+F_z$$

$$\rho\frac{\partial^2 U_\varphi}{\partial t^2}=\frac{\partial}{\partial z}\left(c_{44}\frac{\partial U_\varphi}{\partial z}\right)+\left(\frac{c_{11}-c_{12}}{2}\right)\frac{\partial^2 U_\varphi}{\partial r^2}+F_\varphi.$$

The source terms F_r, F_z, F_φ can be chosen to represent a vertical single-force point source or an explosion point source for the P–SV-wave generation and a single-force point source for the generation of the SH-waves (Alterman & Aboudi 1970).

A partial separation of variables is achieved by replacing the displacement components by functions which are dependent on one of the spatial components and a wave number integration over the other component. Using the finite Hankel transformation for the integration, the

separation formulas are

$$U_r(z, r, t) = \frac{2}{a^2} \sum_{i=1}^{\infty} S(z, k_i, t) \frac{J_1(k_i r)}{|J_1(k_i a)|^2},$$

$$U_z(z, r, t) = \frac{2}{a^2} \sum_{i=1}^{\infty} R(z, k_1, t) \frac{J_0(k_i r)}{|J_1(k_i a)|^2},$$

$$U_\varphi(z, r, t) = \frac{2}{a^2} \sum_{i=1}^{\infty} T(z, k_i, t) \frac{J_0(k_i r)}{|J_1(k_i a)|^2}.$$

The discrete wave number k_i has to be evaluated from $J_0(k_i a) = 0$, where a is the model size in radial direction.

The functions R, S, T describe the dependence of the displacements on the vertical spatial coordinate z and the time t. The dependence on the horizontal spatial coordinate, r, is described by the zero'th and first order Bessel functions. Higher order Bessel functions and more than one set of functions R, S, T are needed in the case of complex sources. The three components of the displacement vector are then coupled over the near-field contribution in the source term (Korn 1985).

Substitution of these expressions for the displacements into the equation of motion leads to the following set of differential equations for R, S, T:

$$\rho S_{tt} = (c_{44} S_z - k_i c_{44} R)_z - k_i c_{13} R_z - k_i^2 c_{11} S + \hat{F}_r,$$

$$\rho R_{tt} = (c_{33} R_z + k_i c_{13} S)_z + k_i c_{44} S_z - k_i^2 c_{44} R + \hat{F}_z,$$

$$\rho T_{tt} = (c_{44} T_z)_z - k_i^2 \left(\frac{c_{11} - c_{12}}{2}\right) T + \hat{F}_\varphi.$$

The subscripts t, z indicate partial derivatives. $\hat{F}_z$, $\hat{F}_r$, $\hat{F}_\varphi$ are the source contributions in the transformed system. These equations can be solved by conventional finite difference methods.

For isotropic media, Korn (1985) derived a second-order finite difference scheme from the wave equation for the homogeneous medium and the boundary conditions using the concept of fictitious grid points. We extended this scheme to allow simulations for transversely isotropic media.

An analysis of numerical anisotropy was carried out by

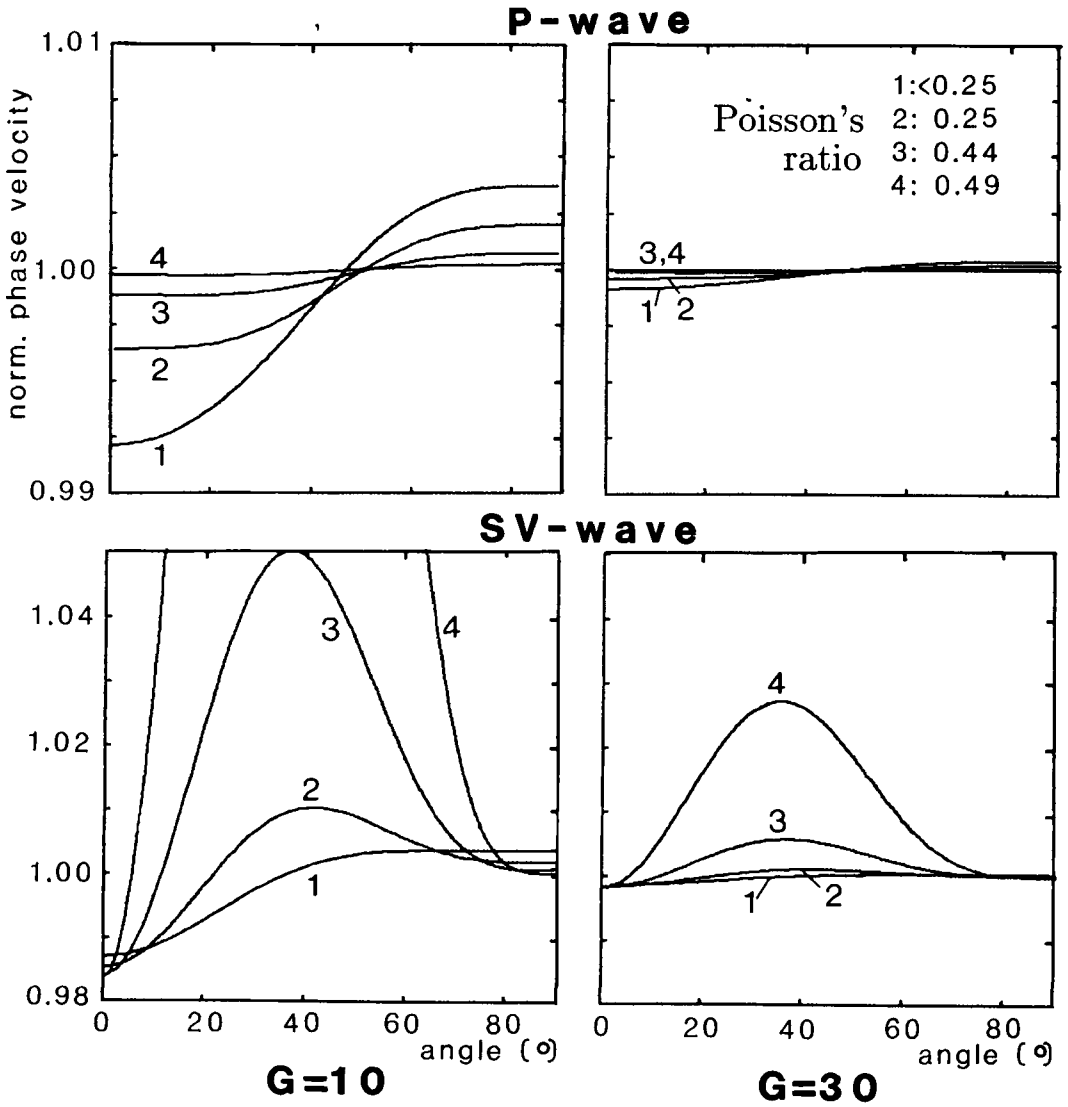

Figure A1. Numerical anisotropy: the influence of the Poisson's ratio on the phase velocities of P- and SV-waves. (G: number of gridpoints per wavelength; the angle of incidence is defined with respect to the vertical direction).

using the method described by Alford, Kelly & Boore (1974). Plane wave solutions were introduced into the finite difference equations for the homogeneous, isotropic medium and the phase velocities for waves incident under different angles were evaluated. We shall not investigate the dependence of numerical anisotropy on the time increment but carry out the analysis using the largest time increment which guarantees stability (critical time step). The effects of the time increment on second-order finite difference results have been investigated, for example by Marfurt (1984).

The numerical anisotropy depends on the number of grid points per wavelength G. Obviously, if the chosen space sampling in the finite difference grid is fine enough, the finite difference solution converges to the error-free solution. However, computational limits are quickly reached when increasing the number of samples. Ten grid points per wavelength is the value for G which is generally regarded as sufficient sampling for finite difference modelling with second-order accuracy. It has to be chosen for the lowest wavelength in the model. In a time-iterating scheme, the lowest wavelength has to be determined from the highest significant frequency (= upper half-power frequency) in the source signal and the lowest shear wave velocity in the model. This choice means that the wavelengths related to lower frequency values are sampled by more than G grid points. For example in the case of a Küpper-wavelet (Küpper 1958) which we used in the modelling, the wavelength related to the predominant frequency is sampled with about $3 \times G$ grid points.

Figure A1 shows the effect of numerical anisotropy on the P- and SV-wave phase velocities. The velocities are normalized with the body wave velocities. We computed the velocity curves for 10 grid points per wavelength and for 30 grid points per wavelength. The velocity curves were also computed for different Poisson's ratios.

The results illustrate that the effect of numerical anisotropy is much larger for shear waves than for compressional waves. For 10 grid points per wavelength in the case of P-waves, the error in the velocity does not exceed 1 per cent for the whole range of Poisson's ratios. It is noticeable that the largest errors occur for low Poisson's ratios. The reverse is true for the velocity errors of the shear wave. In this case the errors increase for higher Poisson's ratios. Except for Poisson's ratios less than 0.25, maxima occur in the SV velocity error curves at approximately 40°. In the case of a Poisson's ratio of 0.44, corresponding to a factor of three between P- and S-wave velocities, the maximum velocity error is 5 per cent. For a Poisson's ratio of 0.49 the maximum error is more than 20 per cent. For many modelling purposes such large errors are unacceptable, especially in cases of large models with long travel paths for the waves. The occurrence of maxima in the shear wave phase velocity curves causes a focusing of wave energy in the direction of maximum phase velocity which is described as being a characteristic of transverse isotropy in rock in the main part of this paper. To avoid these artefacts, the number of grid points has to be increased considerably if Poisson's ratio is high. Using 30 grid points per wavelength the errors are overall less than 0.5 per cent, except for a Poisson's ratio of 0.49.

Figure A2 illustrates the drastic increase in the number of grid points per wavelength required to restrict the maximum shear wave velocity errors to 1, 2 and 3 per cent as Poisson's ratio is increased. Sampling with 10 grid points is certainly sufficient for media with Poisson's ratios of less than 0.4, if an error of 2 or 3 per cent is acceptable for the modelling purpose. But, for the higher Poisson's ratios which often occur in near-surface sedimentary layers, or for more exact solutions, the grid point number has to be much larger. For the modelling of the field case we restricted the velocity error to 1 percent which is one order of magnitude lower than the effect caused by rock anisotropy. We needed 30 grid points per wavelength (as defined above) because of a Poisson's ratio of 0.47.

As the computer time increases with the square of the number of grid points per wavelength it is desirable to use a finite difference scheme which is less or not at all sensitive to the Poisson's ratio. Virieux (1986) has developed an explicit finite difference scheme for the elastodynamic equations which fulfils these requirements. In a forthcoming paper (Kerner 1989) the application of his approach to the Alekseev–Mikhailenko method will be given.

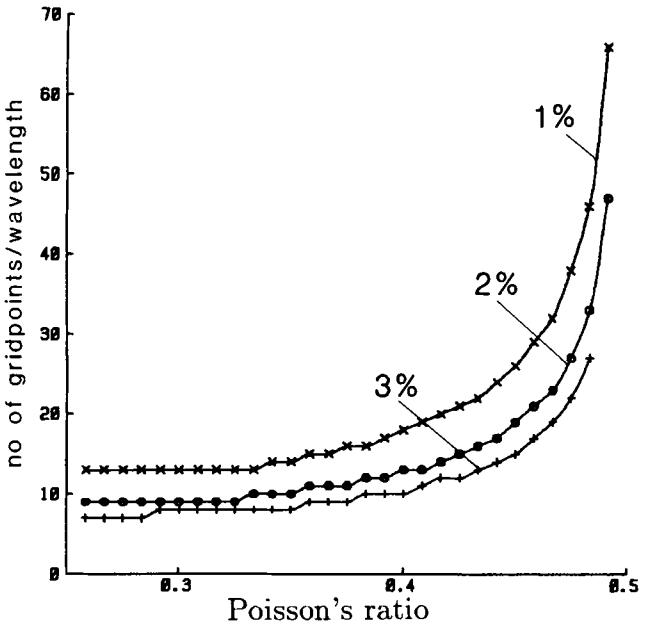

Figure A2. Numerical anisotropy: number of gridpoints per wavelength required to restrict the maximum phase velocity errors to 1, 2 and 3 percent.